The Cryosphere Discuss., 9, 3617–3660, 2015
www.the-cryosphere-discuss.net/9/3617/2015/
doi:10.5194/tcd-9-3617-2015

The Cryosphere
Discussions
Open Access

A new methodology to simulate subglacial deformation of water saturated granular material

A. Damsgaard[1], **D. L. Egholm**[1], **J. A. Piotrowski**[1], **S. Tulaczyk**[2], **N. K. Larsen**[1,3], **and C. F. Brædstrup**[1]

[1]Department of Geoscience, Aarhus University, Aarhus C, Denmark
[2]Department of Earth and Planetary Sciences, University of California, Santa Cruz, California 95064, USA
[3]Centre for GeoGenetics, Natural History Museum of Denmark, University of Copenhagen, 1350 Copenhagen K, Denmark

Received: 16 June 2015 – Accepted: 24 June 2015 – Published: 13 July 2015

Correspondence to: A. Damsgaard (anders.damsgaard@geo.au.dk)

Published by Copernicus Publications on behalf of the European Geosciences Union.

Abstract

The dynamics of glaciers are to a large degree governed by processes operating at the ice–bed interface, and one of the primary mechanisms of glacier flow over soft unconsolidated sediments is subglacial deformation. However, it has proven difficult to constrain the mechanical response of subglacial sediment to the shear stress of an overriding glacier. In this study, we present a new methodology designed to simulate subglacial deformation using a coupled numerical model for computational experiments on grain-fluid mixtures. The granular phase is simulated on a per-grain basis by the discrete element method. The pore water is modeled as a compressible Newtonian fluid without inertia. The numerical approach allows close monitoring of the internal behavior under a range of conditions.

The rheology of a water-saturated granular bed may include both plastic and rate-dependent dilatant hardening or weakening components, depending on the rate of deformation, the material state, clay mineral content, and the hydrological properties of the material. The influence of the fluid phase is negligible when relatively permeable sediment is deformed. However, by reducing the local permeability, fast deformation can cause variations in the pore-fluid pressure. The pressure variations weaken or strengthen the granular phase, and in turn influence the distribution of shear strain with depth. In permeable sediments the strain distribution is governed by the grain-size distribution and effective normal stress and is typically on the order of tens of centimeters. Significant dilatant strengthening in impermeable sediments causes deformation to focus at the hydrologically more stable ice–bed interface, and results in a very shallow cm-to-mm deformational depth. The amount of strengthening felt by the glacier depends on the hydraulic conductivity at the ice–bed interface. Grain-fluid feedbacks can cause complex material properties that vary over time, and which may be of importance for glacier stick-slip behavior.

1 Introduction

The coupled mechanical response of ice, water and sediment can control the flow of glaciers residing on deformable sediment (e.g. Alley et al., 1987; Bindschadler et al., 2001; Clarke, 2005; Bougamont et al., 2011; Turrin et al., 2014). This is clearly expressed by ice streams in Greenland and Antarctica, where low levels of basal friction enable high flow rates. These ice streams are of particular interest, since they are large constituents of the polar ice sheet mass balance (e.g. Rignot and Thomas, 2002).

Although the majority of flow-limiting friction of ice streams terminating into ice shelves is likely provided by ice shelf buttressing (De Angelis and Skvarca, 2003; Rignot et al., 2004; Dupont and Alley, 2005), the disintegration of these ice shelves leaves lateral (Whillans and van der Veen, 1997; Tulaczyk et al., 2000b; Price et al., 2002) and basal friction (Alley, 1993; MacAyeal et al., 1995; Stokes et al., 2007; Sergienko and Hindmarsh, 2013) as the main mechanical components resisting the flow. A fundamental understanding of subglacial dynamics is a requirement for our ability to predict future response of the ice sheets to climate change.

The pressure and flow of pore water in the subglacial bed can influence subglacial deformation in a number of ways. Assuming a Mohr–Coulomb constitutive relation of the basal till strength, an increase in pore water pressure weakens the bed by reducing the effective stress, and this may facilitate basal movement if the driving shear stresses become sufficient to overcome the sediment yield strength (Kamb, 1991; Iverson et al., 1998; Tulaczyk et al., 2000a; Fischer and Clarke, 2001; Kavanaugh and Clarke, 2006).

If the hydraulic diffusivity of the bed is sufficiently low relative to the deformational velocity, a modulation of the pore-water pressure at the ice–bed interface is over time carried into the subglacial bed, resulting in variable internal yield strength and ultimately variable shear strain rates with depth (Tulaczyk, 1999; Tulaczyk et al., 2000a; Kavanaugh and Clarke, 2006). Owing to local volumetric changes, variations from the hydrostatic fluid pressure distribution can be created inside the sediment by the onset and halt of granular deformation. This influences the local effective pressure and, in turn, the sediment yield strength (e.g. Iverson et al., 1998).

In the case of non-planar ice-bed geometry excess pore-water pressures can develop on the stoss side of objects ploughing through a subglacial bed (Iverson et al., 1994; Iverson, 1999; Thomason and Iverson, 2008). The elevated pore-water pressure weakens the sediment by lowering the effective stress, resulting in a net strain-rate weakening rheology (e.g. Iverson et al., 1998; Fischer et al., 2001; Clark et al., 2003; Iverson, 2010), which has been associated with the stick-slip behavior of Whillans Ice Stream (Winberry et al., 2009).

Early field studies suggested a strain-rate strengthening Bingham or slightly non-linear viscous rheology of till (Boulton and Hindmarsh, 1987), which has been used to simplify analytical and numerical modeling of till mechanics (e.g. Alley et al., 1987; Hindmarsh, 1998; Fowler, 2000). Laboratory studies have, however, favored the notion of till having a plastic, Mohr–Coulomb rheology, with a very small rate-dependence in the case of a critical state deformation (Kamb, 1991; Iverson et al., 1998; Tulaczyk et al., 2000a; Rathbun et al., 2008). This Mohr–Coulomb rheology is also supported by field investigations (Truffer et al., 2000; Kavanaugh and Clarke, 2006). On the other hand, a rate-weakening rheology is expected in the case where obstacles plough through a soft and deformable bed (Iverson et al., 1994; Iverson, 1999).

Both viscous and plastic rheologies are expected end-members of particle–fluid mixtures, dependent on the deformational rate, fluid viscosity, fluid-solid volumetric fraction and confining stresses. The low viscosity of water does, however, make it easy to deform even under high strain rates and can only be expected to influence the overall rheology of subglacial materials in a few select scenarios (e.g. Iverson, 2010). The mechanics of coupled granular-fluid mixtures have previously been numerically investigated for studies of fluidized beds (e.g. Anderson and Jackson, 1967; Gidaspow et al., 1992; Hoomans et al., 1996; Xu and Yu, 1997; McNamara et al., 2000; Feng and Yu, 2004; Jajcevic et al., 2013), the stability of inclined, fluid-immersed granular materials (e.g. Topin et al., 2011; Mutabaruka et al., 2014), mechanics during confined defor-

TCD
9, 3617–3660, 2015

mation (e.g. Goren et al., 2011; Catalano et al., 2014), debris flow (e.g. Hutter et al., 1994; Mangeney et al., 2007; Goren et al., 2011) and for the design of industrial components, e.g. hydrocyclones (e.g. Wang et al., 2007; Zhou et al., 2010), or silos and hoppers (Kloss et al., 2012).

This study explores the interaction between the fluid and granular phases in water-saturated consolidated particle assemblages undergoing slow shear deformation. A dry granular assemblage deforms rate-independently in a pseudo-static manner when deformational rates are sufficiently low (GDR-MiDi, 2004; Damsgaard et al., 2013). The particle–fluid mixture is in this study sheared with velocities and stresses comparable to those found in subglacial settings. The computational approach allows for investigating the internal granular mechanics and feedbacks during progressive shear deformation.

In the following section, we present the details of the numerical implementation of particle–fluid flow, and describe the experimental setup. We then present and discuss the modeled deformational properties of the particle–fluid mixture. Finally, we analyze how the fluid influences formation of shear zones and under which conditions deformation is rate dependent.

2 Methods

2.1 The granular model

We use the discrete element method (DEM) (Cundall and Strack, 1979) to simulate the granular deformation. With the DEM, particles are treated as separate, cohesion-less entities, which interact by soft-body deformation defined by a prescribed contact law. The contact mechanics are micro-mechanically parameterized. The temporal evolution is handled by integration of the momentum equations of translation,

$$m^i \frac{\partial^2 \boldsymbol{x}^i}{\partial t^2} = \underbrace{m^i \boldsymbol{g}}_{\text{Gravity}} + \overbrace{\sum_j \left(\boldsymbol{f}_\mathrm{n}^{ij} + \boldsymbol{f}_\mathrm{t}^{ij} \right)}^{\text{Contact forces}} + \boldsymbol{f}_\mathrm{i}^i \tag{1}$$

and rotation:

$$I^i \frac{\partial^2 \boldsymbol{\Omega}^i}{\partial t^2} = \underbrace{\sum_j \left(- \left(r^i + \frac{\delta_\mathrm{n}^{ij}}{2} \right) \boldsymbol{n}^{ij} \times \boldsymbol{f}_\mathrm{t}^{ij} \right)}_{\text{Contact torques}} \tag{2}$$

i and j are particle indexes, m is the particle mass, I is the particle rotational inertia, $\boldsymbol{x}$ and $\boldsymbol{\Omega}$ are linear and rotational particle positions, respectively. $\boldsymbol{f}_\mathrm{n}$ and $\boldsymbol{f}_\mathrm{t}$ are the interparticle contact force vectors in the normal and tangential direction relative to the contact interface, and $\boldsymbol{f}_\mathrm{i}$ is the fluid-particle interaction force (Fig. 1). $\boldsymbol{n}$ is the inter-particle normal vector, and δ_n is the inter-particle overlap distance at the contact. The inter-particle contact forces are determined by a linear-elastic contact model. The magnitude of the tangential force $\boldsymbol{f}_\mathrm{t}$ is limited by the Coulomb frictional coefficient μ (Cundall and Strack, 1979; Luding, 2008; Radjaï and Dubois, 2011; Damsgaard et al., 2013):

$$\boldsymbol{f}_\mathrm{n}^{ij} = -k_\mathrm{n} \delta_\mathrm{n}^{ij} \boldsymbol{n}^{ij} \text{ and } \boldsymbol{f}_\mathrm{t}^{ij} = -\max \left\{ k_\mathrm{t} \|\boldsymbol{\delta}_\mathrm{t}^{ij}\|, \mu \|\boldsymbol{f}_\mathrm{n}^{ij}\| \right\} \frac{\boldsymbol{\delta}_\mathrm{t}^{ij}}{\|\boldsymbol{\delta}_\mathrm{t}^{ij}\|} \tag{3}$$

The vector $\boldsymbol{\delta}_\mathrm{t}$ is the tangential displacement on the inter-particle interface when corrected for contact rotation. In the case of slip, the length of $\boldsymbol{\delta}_\mathrm{t}$ is adjusted to a length consistent with Coulomb's condition ($\|\boldsymbol{\delta}_\mathrm{t}\| = -\mu \|\boldsymbol{f}_\mathrm{n}\| / k_\mathrm{t}$) (Luding, 2008; Radjaï and Dubois, 2011). The linear elasticity allows temporal integration with a constant time step length Δt.

2.2 The fluid model

The inter-particle fluid is handled by conventional continuum computational fluid dynamics (CFD). The implementation follows the compressible Darcian flow model presented by Goren et al. (2011). This approach was favored over a full Navier–Stokes solution of fluid flow (Gidaspow, 1994; Zhu et al., 2007; Zhou et al., 2010; Kloss et al., 2012) since it allows for convenient parameterization of the hydrological permeabilities. The model assumes insignificant fluid inertia, which is appropriate for the subglacial setting.

The volumetric fraction of the fluid phase (the porosity, ϕ) is incorporated in the Eulerian formulations of the compressible continuity equation and momentum equation using the local average method (Anderson and Jackson, 1967; Xu and Yu, 1997). The Darcy constitutive equation is used for conserving momentum (Eq. 5) (McNamara et al., 2000; Goren et al., 2011):

$$\frac{\partial p_\mathrm{f}}{\partial t} = \underbrace{\frac{1}{\beta_\mathrm{f}\phi\mu_\mathrm{f}}\nabla\cdot\left(k\nabla^2 p_\mathrm{f} + \nabla p_\mathrm{f}\cdot\nabla k\right)}_{\text{Spatial diffusion}} + \underbrace{\frac{1}{\beta_\mathrm{f}\phi(1-\phi)}\left(\frac{\partial\phi}{\partial t} + \bar{\boldsymbol{v}}_\mathrm{p}\cdot\nabla\phi\right)}_{\text{Particle forcing}} \tag{4}$$

$$(\boldsymbol{v}_\mathrm{f} - \boldsymbol{v}_\mathrm{p})\phi = -\frac{k}{\mu_\mathrm{f}}\nabla p_\mathrm{f} \tag{5}$$

where $\boldsymbol{v}_\mathrm{f}$ is the fluid velocity, $\boldsymbol{v}_\mathrm{p}$ is the particle velocity, k is the hydraulic permeability, β_f is the adiabatic fluid compressibility and μ_f is the dynamic fluid viscosity. The continuity equation (Eq. 4) is in the form of a transient diffusion equation with the forcing term acting as a source/sink for the fluid pressure. The pressure, p_f, is the pressure deviation from the hydrostatic pressure distribution. This pressure deviation is sometimes referred to as the *excess pressure*. We refrain from using this term, as it may be misleading for pressures that are smaller than the hydrostatic value.

The simulation domain is discretized in a regular rectilinear orthogonal grid. The pressure is found using the Crank–Nicolson method of mixed explicit and implicit temporal integration, which is unconditionally stable and second-order accurate in time and space (e.g. Patankar, 1980; Ferziger and Perić, 2002; Press et al., 2007). The implicit solution is obtained using the iterative Jacobi relaxation method (e.g. Ferziger and Perić, 2002; Press et al., 2007; Gerya, 2010), which is light on memory requirements and ideal in terms of parallelism for our graphics processing unit (GPU) implementation, although not optimal in terms of convergence. The numerical solution is continuously checked by the Courant–Friedrichs–Lewy condition (Courant et al., 1967). The partial derivatives are approximated by finite differences.

2.3 The granular-fluid coupling

The particle and fluid algorithms interact by direct forcings (Eqs. 1 and 4) and through measures of porosity and permeability (Tsuji et al., 1992, 1993; Xu et al., 2001; Zhu et al., 2007; Goren et al., 2011).

2.3.1 Porosity

The local porosity is determined at the fluid cell center. For a cell with a set of N grains in its vicinity, it is determined by inverse-distance weighting the grains using a bilinear interpolation scheme (McNamara et al., 2000; Goren et al., 2011). The weight function s has the value 1 at the cell center and linearly decreases to 0 at a distance equal to the cell width (Δx, Fig. 2):

$$\phi(\boldsymbol{x}_\mathrm{f}) = 1 - \frac{\sum_{i \in N} s^i V_\mathrm{g}^i}{\Delta x^3} \tag{6}$$

$$s^i = \begin{cases} \prod_{d=1}^{3} \left[1 - \frac{|\boldsymbol{x}_d^i - \boldsymbol{x}_{\mathrm{f},d}|}{\Delta x} \right] & \text{if } |\boldsymbol{x}_1^i - \boldsymbol{x}_{\mathrm{f},1}|, |\boldsymbol{x}_2^i - \boldsymbol{x}_{\mathrm{f},2}|, |\boldsymbol{x}_3^i - \boldsymbol{x}_{\mathrm{f},3}| < \Delta x \\ 0 & \text{otherwise} \end{cases} \tag{7}$$

Δx^3 is the fluid cell volume, and $\boldsymbol{x}_\mathrm{f}$ is the cell center position. Π is the product operator. The average grain velocity at the cell center is found using the same weighting func-

TCD
9, 3617–3660, 2015

tion described above (Eq. 7). Additionally, large grains contribute to the velocity with a greater magnitude:

$$\overline{\boldsymbol{v}}(\boldsymbol{x}_\mathrm{f}) = \frac{\sum_{i \in N} s^i V_\mathrm{g}^i \boldsymbol{v}^i}{\sum_{i \in N} s^i} \tag{8}$$

The change in porosity is the main forcing the particles excert onto the fluid (Eq. 5). At time step n it is estimated by central differences for second-order accuracy:

$$\left[\frac{\partial \phi}{\partial t}\right]^n \approx \frac{\phi^{n+1} - \phi^{n-1}}{2\Delta t} \tag{9}$$

The porosity at $n+1$ is found by estimating the upcoming particle positions from temporal integration of their current positions and velocities.

2.3.2 Permeability

Significant empirical evidence has been gathered about the proportionality between grain size and hydraulic properties of sediments (e.g. Hazen, 1911; Kozeny, 1927; Carman, 1937; Krumbein and Monk, 1943; Harleman et al., 1963; Schwartz and Zhang, 2003). The Kozeny–Carman estimation of permeability k is commonly used and of the form,

$$k = \frac{d^2}{180} \frac{\phi^3}{(1-\phi)^2} \tag{10}$$

where d is the representative grain diameter. Due to constrains on the computational time step we are unable to simulate fine grain sizes with realistic elastic properties within a reasonable time frame. In order to give a first-order estimate of the deformational behavior of fine-grained sediments, we therefore use a modified version of

TCD
9, 3617–3660, 2015

the above relationship, where the permeability varies as a function of the porosity and a predefined permeability pre-factor k_c:

$$k = k_c \frac{\phi^3}{(1-\phi)^2} \tag{11}$$

Using this approach we can simulate large particles with the hydrological properties of fine-grained materials, while retaining the effect of local porosity variations on the intrinsic permeability. We do note, however, that the dilative magnitude during deformation is likely different for clay materials due to their plate-like shape. Sediments with a considerable amount of arbitrarily oriented clay minerals are likely to compact during deformation as the clay particles align to accommodate shear strain.

2.3.3 Particle–fluid interaction

The dynamic coupling from the pore fluid to the solid particles acts through the particle–fluid force ($\boldsymbol{f}_i$) in Eq. (1). Our implementation of this coupling follows the procedure outlined by Xu and Yu (1997); Feng and Yu (2004) and Zhou et al. (2010) (scheme 3).

In a complete formulation, the interaction force on particles is composed of the drag force, determined by semi-empirical relationships (Ergun, 1952; Wen and Yu, 1966; Gidaspow et al., 1992; Di Felice, 1994), the pressure gradient force, the viscous force, as well as weaker interaction forces caused by particle rotation (Magnus force), lift forces on the particles caused by fluid velocity gradients (Saffman force), and interaction forces caused by particle acceleration (virtual mass force) (Zhou et al., 2010).

However, initial tests using a full Navier–Stokes solution for the fluid phase showed us that the pressure gradient force was by far the dominant interaction force in our pseudo-static shear experiments. The drag force was the second-most important force, but two orders of magnitude weaker than the pressure gradient force. Since we neglect fluid inertia, we included only the pressure gradient force. This force pulls particles towards relatively low fluid pressures and pushes them away from relatively high pressures.

The fluid pressure in our model records the pressure difference from the hydrostatic pressure. For this reason we add a term to the pressure gradient force, which describes the buoyancy of a fully submerged particle as the weight of the displaced fluid:

$$\boldsymbol{f}_{\mathrm{i}} = -V_{\mathrm{g}} \nabla p_{\mathrm{f}} - \rho_{\mathrm{f}} V_{\mathrm{g}} \boldsymbol{g} \tag{12}$$

V_{g} is the volume of the particle, ρ_{f} is the fluid density and $\boldsymbol{g}$ is the vector of gravitational acceleration. The particle–fluid interaction force is added to the sum of linear forces per particle (Eq. 1). The particle force is not added to the fluid momentum equation (Eq. 4) since fluid inertia is ignored. The fluid is instead forced by variations in porosity.

2.4 Computational experiments

The computational fluid dynamics (CFD) algorithm is implemented in CUDA C (NVIDIA, 2013) in order to allow a direct integration with the GPU-based particle solver. The coupled particle–fluid code is free software (source code available at https://github.com/anders-dc/sphere), licensed under the GNU Public License v.3. The simulations were performed on a GNU/Linux system with a pair of NVIDIA Tesla K20c GPUs. The experimental results are visualized using ParaView (Henderson et al., 2007) and Matplotlib (Hunter, 2007).

The experimental setup is a rectangular volume (Fig. 3) where a fluid-saturated particle assemblage deforms due to forcings imposed at the outer boundaries. We deform the consolidated material by a constant-rate shearing motion in order to explore the macro-mechanical shear strength under different conditions.

To determine the effects of the pore water, we perform experiments with and without fluids, and for the experiments with fluids present, the permeability pre-factor k_{c} is varied to constrain the effect of the hydraulic conductivity and diffusivity on the overall deformation style. The low value used for k_{c} ($3.5 \times 10^{-15}\,\mathrm{m}^2$) results in an intrinsic permeability of $k = 1.9 \times 10^{-16}\,\mathrm{m}^2$ for a porosity of 0.3 (Eq. 11). The highest value ($k_{\mathrm{c}} = 3.5 \times 10^{-13}\,\mathrm{m}^2$) matches a permeability of $1.9 \times 10^{-14}\,\mathrm{m}^2$. These two end-member

TCD
9, 3617–3660, 2015

permeabilities roughly correspond to what Iverson et al. (1997a) and Iverson et al. (1998) estimated for the clay-rich Two Rivers till and the clay-poor Storgläciaren till, respectively.

The lower boundary is impermeable, and a fixed fluid pressure is specified for the top boundary. These boundary conditions imply that the simulated ice–bed interface is a relatively permeable zone with rapid diffusion of hydrological pressure, which is likely for subglacial beds with low permeability (e.g. Alley, 1989; Creyts and Schoof, 2009; Kyrke-Smith et al., 2014). In coarse-grained tills it is likely that the subglacial till diffusivity exceeds the hydraulic diffusivity at the ice bed interface. The lateral boundaries are periodic (wrap-around). If a particle moves outside the grid on the right side it immediately reappears on the left side. Likewise, particle pairs can be in mechanical contact although placed on opposite sides of the grid at the periodic boundaries.

The particle size distribution is narrow compared to that of subglacial tills, which often display a fractal size distribution (e.g. Hooke and Iverson, 1995). Fractal size distributions minimize internal stress heterogeneities (Hooke and Iverson, 1995; Iverson et al., 1996), but, in the absence of grain crushing, an assemblage with a wide particle size distribution dilates from a consolidated state with the same magnitude as assemblages with a narrow particle size distribution (Morgan, 1999) and displays the same frictional strength (Morgan, 1999; Mair et al., 2002; Mair and Hazzard, 2007). The comparable dilation magnitude justifies the computationally efficient narrow particle size distribution used here. As previously noted, shear zones in clay-rich materials can compact during shear due to preferential parallel alignment, which is not possible to capture with the methodology presented here.

The simulated particle size falls in the gravel category of grain size. The large size allows us to perform the temporal integration with larger time steps (Radjaï and Dubois, 2011; Damsgaard et al., 2013). The frictional force between two bodies is independent of their size (Amontons' second law) but is proportional to the normal force on the contact interface (Mitchell and Soga, 2005), as reflected in the contact law in the discrete element method (Eq. 3). We prescribe the normal forcing at the boundary as a normal stress, which implies that the normal force exerted onto a particle assemblage at the boundaries scales with domain size. For a number of total particles in a given packing configuration the ratio between particle size and inter-particle force is constant, which causes the shear strength to be independent of simulated particle size. This scale-independence is verified in laboratory experiments, where the granular shear strength of non-clay materials is known to be mainly governed by grain shape and surface roughness instead of grain size (Schellart, 2000; Mitchell and Soga, 2005).

2.4.1 Experiment preparation and procedure

The particles are initially placed in a dry, tall volume, from where gravity allows them to settle into a dense state. The particle assemblage is then consolidated by moving the fluid-permeable top wall downwards until the desired level of consolidation stress is reached for an extended amount of time. The same top wall is thereafter used to shear the material in a fluid-saturated state (Fig. 3).

For the shear experiments, the uppermost particles are forced to move with the top wall at a prescribed horizontal velocity (Fig. 3). The particles just above the bottom wall are prescribed to be neither moving or rotating. The micro-mechanical properties and geometrical values used are listed in Table 1.

2.4.2 Scaling of the shear velocity

The heavy computational requirements of the discrete element method necessitates upscaling of the shearing velocity in order to reach a considerable shear strain within a manageable length of time. Temporal upscaling does not influence the mechanical behavior of dry granular materials, as long as the velocity is below a certain limiting velocity (GDR-MiDi, 2004; Damsgaard et al., 2013; Gu et al., 2014). The shearing velocity used here ($2.32 \times 10^{-2}\,\mathrm{m\,s^{-1}}$), although roughly three orders of magnitude greater than the velocities observed in subglacial environments (e.g. $316\,\mathrm{m\,a^{-1}} = 10^{-5}\,\mathrm{m\,s^{-1}}$), guarantees quasi-static, rate-independent deformation in the granular phase, identical to the behavior at lower strain rates. The particle inertia parameter, I, quantifies the influence of grain inertia in dry granular materials (GDR-MiDi, 2004). Values of I below 10^{-3} correspond to pseudo-static and rate-independent shear deformation in dry granular materials. I has a value of 1.7×10^{-4} in the shear experiments of this present study.

The fluid phase needs separate treatment in order to correctly resolve slow shear behavior at faster shearing velocities. This behavior is achieved by linearly scaling the fluid dynamic viscosity with the relationship between actual shearing velocity and the reference glacial sliding velocity. By decreasing the viscosity the fluid is allowed to more quickly adjust to external and internal forcings. The velocity scaling adjusts the time-dependent parameters of hydraulic conductivity and diffusivity correctly. The intrinsic permeability k is time-independent, and the values produced here are directly comparable with real geological materials. The fluid viscosity is scaled to a lower value of 1.797×10^{-6} Pa s, consistent with the scaling factor used for the shearing velocity. We test the influence of shearing rate by varying this parameter.

3 Results

First we investigate the strain-rate dependence of the sediment strength and dilation by shearing a relatively impermeable sediment ($k_c = 3.5 \times 10^{-15}$ m^2) at different shear velocities. The shear velocity directly influences the magnitude of the peak shear strength, dilation and internal fluid pressure (Figs. 4 and 5). At relatively large shearing velocities the dilation rate exceeds the pore-pressure diffusion rate, and the internal pressure reduction strengthens the material. At lower shearing velocities the material is substantially weaker due to a decreased dilation rate, where the pore pressure diffusion has more time to adjust to the volumetric changes in the shear zone.

At the reference shearing velocity the peak shear frictional strength is 0.71, which corresponds to 14 kPa at an effective stress of 20 kPa (Figs. 4, top left, and 6). When sheared a hundred times slower, the peak shear friction has decreased to 0.62, corresponding to 12 kPa (Figs. 4, top right, and 6). The peak values are measured during the transition from the dense and consolidated pre-failure state to the critical state where a shear zone is fully established. This transition is characterized by rapid dilation due to porosity increases in the shear zone (Fig. 4, middle). During fast shearing velocities the volumetric change outpaces the diffusion of fluid pressure, causing the internal pore-water pressure in the shear zone to decline (Figs. 4, bottom and 5). Dilatant hardening causes the peak shear strength to increase at large shear velocities (Fig. 6), while the strength reduces to the pure granular strength for lower velocities.

In this model framework, adjusting the hydraulic permeability of the same coarse sediment leads to similar conditional strengthening as shearing the sediment at different rates (Fig. 7). Without fluids (the dry experiment), the peak shear friction (Fig. 7, left) is relatively low and the shear stress is dominated by high-frequency fluctuations. The fluid-saturated experiment with the relatively high permeability ($k_c = 3.5 \times 10^{-13}$ m^2) has similar shear strength, but the high-frequency oscillations in shear friction are reduced by the fluid presence. The dilation is similar to the dry experiment, but with slightly decreased magnitude. The mean fluid pressure deviation from hydrostatic values (Fig. 7, bottom left) is close to zero. The low-permeable experiment (Fig. 7, right) is characterized by the largest initial peak strength, and lowest magnitude of dilation. Compared to the other experiments, the dilation reaches its maximum values at lower shear strain. The fluid pressure decreases almost instantaneously at first, whereafter it equilibrates towards the hydrostatic value (0 Pa).

At constant shearing rate with different permeabilities (Fig. 8, top) or at variable shearing rates with constant permeability (Fig. 8, bottom), we observe that pore water dynamics have a significant effect on the distribution of strain. The presence of pore water causes a more shallow deformational profile. Progressively lowering the permeability or increasing the shear velocity decreases the deformational depth.

The effects of the fluid are visible at different depths within the deforming material (Figs. 9 and 10). The deformation is pervasive with depth for the relatively permeable experiment (Fig. 9 top), and the fluid pressures deviate only slightly from the hydrostatic

TCD
9, 3617–3660, 2015

values (red). The relatively small pressure gradients cause only weak fluid forces on the particles in this experiments. Contrasting these results, deformation is in the impermeable experiment primarily governed by decoupling of the top wall and the particles in the bed below (Figs. 9 and 10, bottom).

Differences in hydraulic permeability influence the dynamics of the fluid over time, as illustrated in Fig. 11. The fluid pressures in the permeable material (top) are initially predominantly negative, reflecting the increasing dilation (Fig. 7, middle). In the critical state (after a shear strain value of 0.1), the fluid pressures fluctuate around the hydrostatic value (0 Pa).

4 Discussion

4.1 Strain-rate dependency

Several studies have highlighted the importance of feedbacks between the solid and fluid phases during granular deformation (e.g. Iverson et al., 1994, 1997b, 1998; Pailha et al., 2008; Iverson, 2010; Rondon et al., 2011; Mutabaruka et al., 2014). A shear-rate dependency in a grain-fluid mixture can only originate from the fluid phase, since dry granular materials deform rate-independently under pseudo-static shear deformation (GDR-MiDi, 2004; Damsgaard et al., 2013). Rate dependency emerges, however, as soon as the flow of viscous pore fluids starts to influence the solid phase.

Water has a relatively low viscosity, which implies that the shear stress required to deform the fluid phase alone is extremely low. The fluid phase does however influence the bulk rheology if diffusion of fluid pressures is limited relative to volumetric forcing rates, as in a rapidly deforming but relatively impermeable porous material. The coupled particle–fluid interactions cause the material to respond as a low-pass filter when forced with changes in volume and porosity. The reequilibration of pressure anomalies depends on the volumetric strain rate, water viscosity and material permeability. Any

TCD
9, 3617–3660, 2015

forcing that affects local porosity causes the material to respond in part like a viscous dashpot due to internal fluid flow.

4.2 Dilatant hardening: effects on sediment strength and deformation depth

When deformed, granular materials often undergo volumetric changes in order to attain the optimal packing for continuous deformation (e.g. Schofield and Wroth, 1968). Shear zones within dense granular materials (normally consolidated) typically expand (Fig. 7, middle) in a process known as Reynolds dilation (Reynolds, 1885; Mead, 1925). The pore-volume increase internally in the shear zone causes a local reduction in pore-water pressure, and a deviation from the hydrostatic pressure distribution. The appearance of hydraulic gradients drives fluid flow into the shear zone. Considering the Mohr–Coulomb constitutive relation for till rheology, the reduction of pore-water pressure reduction increases the effective stress, which in turn strengthens the material in the shear zone (Fig. 12). In our results, the particles are pushed towards the shear zone by the pressure gradient force (Fig. 13). The tangential strength of inter-particle contacts is in the DEM determined by Coulomb friction (Eq. 3), which implies a linear correlation between contact normal force and tangential contact strength. Heavily loaded particle contacts are thus less likely to slip, and chains of particles with strong contacts cause increased resistance to deformation (Damsgaard et al., 2013). The convergence of particles strengthens the inter-particle contacts and increases the shear friction until hydrostatic pressure conditions are reestablished.

The dilative strengthening requires sufficiently low hydraulic diffusivities relative to the shear zone dilation rate (e.g. Iverson et al., 1997b; Moore and Iverson, 2002; Iverson, 2010). Dilation ceases when a sediment reaches the critical state. Owing to the granularity of the material, the vertical strain rate displays small fluctuations around levels corresponding to the critical state value. The small volumetric oscillations create new fluid-pressure deviations from the hydrostatic value, which slightly weaken or strengthen the sediment (Fig. 7, top, and Goren et al., 2011). In cases where the shear stress is close to the sediment shear strength, the hardening may be sufficient to stabilize patches of the bed (Piotrowski, 1987).

The granular model applied here is not able to reproduce the shear-induced compaction that clay-rich materials can display during early shear (e.g. Dewhurst et al., 1996), but we can speculate about the rheological consequences. The compaction causes increased pore-water pressure in the shear zone, in cases where the volumetric change exceeds the time scale of pore-water pressure diffusion. Some of the compressive stress normal to the shear zone orientation is consequentially reduced, which decreases the material strength. The reduction of strength due to compaction is rate-dependent like the dilative hardening.

The shear zone thickness is in our experiments heavily influenced by the dilatant hardening where a low permeability causes extremely localized failure at the upper moving interface (Figs. 8 and 9, left). This is consistent with the laboratory results by Iverson et al. (1997a), where the shear zone in the coarse-grained Storgläciaren till in all cases was wider than the shear zone of the fine-grained Two Rivers till. The velocity profile of the shear zone determines the material flux. A shallower deformation depth and a lower subglacial sediment transport rate is thus to be expected from subglacial shearing of compacted, low-permeable sediments, relative to permeable counterparts. These results are consistent with observations of very shallow deformation of subglacial tills with a relatively low permeability (Engelhardt and Kamb, 1998; Piotrowski et al., 2004).

Our results demonstrate how the interplay between the solid and fluid phases can influence the sediment strength. Pore-water pressures decrease during deformation, and shear strength increases until deformation ceases or the critical state is reached. Once the local and regional hydraulic system recovers from the pore-pressure reduction, the sediment strength is once again reduced and a new deformation phase may be initiated (Fig. 14). The magnitude of strengthening is dictated by the ability of the subglacial hydrological system to accommodate reductions in pressure at the ice–bed interface (Fig. 15).

A variable shear strength of the till influences ice flow if the basal shear stress is in the range of the strength values. Since surface slopes of ice streams are low, driving stresses tend to be low as well. Inferred values of driving stresses at the Northeast Greenland ice stream (Joughin et al., 2001), Whillans Ice Stream and ice plain (Engelhardt and Kamb, 1998), and Pine Island Glacier (Thomas et al., 2004) lie within the range of 2 to 23 kPa (Alley and Whillans, 1991; Cuffey and Paterson, 2010), and are thus potentially sensitive to the variability in till strength. If the glacier moves with variable velocities in a stick-slip or surging manner, periods of stagnant ice flow may consolidate and strengthen the sediment, in effect delaying the following slip event (Iverson, 2010).

5 Conclusions

We numerically simulate a two-way coupled particle–fluid mixture under pseudo-static shear deformation. The grains are simulated individually by the discrete element method, while the fluid phase is treated as a compressible and slowly flowing fluid adhering to Darcy's law. The fluid influences the particles through local deviations from the hydrostatic pressure distribution. Due to the extremely low viscosity of water, the deformational behavior of dense granular material is governed by inter-grain contact mechanics. The porosity of a granular packing evolves asymptotically towards a constant value when deformed. Changes in porosity cause deviations from the hydrostatic pressure if the rate of porosity change exceeds the rate of pressure diffusion. The rate of pressure diffusion is governed by the fluid viscosity, the local porosity and the hydraulic permeability. Low fluid pressures developing due to sediment dilation cause a volumetric contraction in the granular phase which increases the stress between particles, in turn increasing the strength of individual grain contacts. The magnitude of the strengthening effect is rate-dependent, and increases with shear velocity and decreases with increasing hydraulic permeability. The resulting rheology is perfect-plastic for permeable or slowly deforming tills while rate-dependent dilative strengthening contributes to the material strength during early stages of fast deformation of impermeable and dilating tills. If the till is clay-rich, compaction due to microfabric development in the shear zone is expected to weaken the sediment, causing a rate-weakening with increased shear rate until the excess pressures are reduced by hydraulic diffusion.

We furthermore show that for a fast shear velocity ($732\,\mathrm{m\,a^{-1}}$) permeable sediments are only weakly influenced by the fluid phase, resulting in little shear strengthening and a deep decimeter-scale deformation dictated by the normal stress and grain sizes. Impermeable and consolidated sediments display slight dilatant strengthening at high shear velocity. The strengthening causes deformation to focus at the ice–bed interface where pore-water pressures are higher and relatively constant. The depth of deformation is then on the centimeter-to-millimeter scale. Actively deforming patches in the subglacial mosaic of deforming and stable spots act as sinks for meltwater and can cause substantial thinning of a water-film at the ice–bed interface. If the subglacial shearing movement halts, the sediment gradually weakens as the fluid pressure readjusts to the hydrostatic value. The temporal changes in sediment strength may explain observed variability in glacier movement.

Acknowledgements. Anders Damsgaard benefited from discussions with Jean-Yves Delenne, Hans Petter Langtangen, Kenni Dinesen Petersen, Keld Rømer Rasmussen, Liran Goren, and Jenny Suckale during model development and application. This research was funded by the Danish Council for Independent Research under the Sapere Aude programme.

References

Alley, R. B.: Water-pressure coupling of sliding and bed deformation: I. Water system, J. Glaciol., 35, 108–118, 1989. 3628

Alley, R. B.: In search of ice-stream sticky spots, J. Glaciol., 39, 447–454, 1993. 3619

Alley, R. B. and Whillans, I. M.: Changes in the West Antarctic ice sheet, Science, 254, 959–963, 1991. 3635

Alley, R. B., Blankenship, D. D., Rooney, S. T., and Bentley, C. R.: Till beneath ice stream B 4. A coupled ice-till flow model, J. Geophys. Res., 92, 8931–8940, 1987. 3619, 3620

Anderson, T. B. and Jackson, R.: A fluid mechanical description of fluidized beds, Ind. Eng. Chem., 6, 527–539, 1967. 3620, 3623
Bindschadler, R., Bamber, J., and Anandakrishnan, S.: Onset of streaming flow in the siple coast region, West Antarctica, in: The West Antarctic Ice Sheet: Behavior and Environment, American Geophysical Union, John Wiley & Sons, Ltd, Hoboken, New Jersey, USA, 123–136, 2001. 3619
Bougamont, M., Price, S., Christoffersen, P., and Payne, A. J.: Dynamic patterns of ice stream flow in a 3-D higher-order ice sheet model with plastic bed and simplified hydrology, J. Geophys. Res.-Earth, 116, F04018, doi:10.1029/2011JF002025, 2011. 3619
Boulton, G. S. and Hindmarsh, R. C. A.: Sediment deformation beneath glaciers: rheology and geological consequences, J. Geophys. Res., 92, 9059–9082, 1987. 3620
Carman, P. C.: Fluid flow through granular beds, Trans. Inst. Chem. Eng., 15, 150–166, 1937. 3625
Catalano, E., Chareyre, B., and Barthélémy, E.: Pore-scale modeling of fluid-particles interaction and emerging poromechanical effects, Int. J. Numer. Anal. Met., 38, 51–71, 2014. 3621
Clark, C. D., Tulaczyk, S. M., Stokes, C. R., and Canals, M.: A groove-ploughing theory for the production of mega-scale glacial lineations, and implications for ice-stream mechanics, J. Glaciol., 49, 240–256, 2003. 3620
Clarke, G. K. C.: Subglacial processes, Annu. Rev. Earth Pl. Sc., 33, 247–276, 2005. 3619
Courant, R., Friedrichs, K., and Lewy, H.: On the partial difference equations of mathematical physics, IBM J. Res. Dev., 11, 215–234, 1967. 3624
Creyts, T. T. and Schoof, C. G.: Drainage through subglacial water sheets, J. Geophys. Res.-Earth, 114, 2156–2202, doi:10.1029/2008JF001215, 2009. 3628
Cuffey, K. M. and Paterson, W. S. B.: The Physics of Glaciers, Elsevier, Amsterdam, Netherlands, 4, 693, 2010. 3635
Cundall, P. A. and Strack, O. D. L.: A discrete numerical model for granular assemblies, Geotechnique, 29, 47–65, 1979. 3621, 3622
Damsgaard, A., Egholm, D. L., Piotrowski, J. A., Tulaczyk, S., Larsen, N. K., and Tylmann, K.: Discrete element modeling of subglacial sediment deformation, J. Geophys. Res.-Earth, 118, 2230–2242, 2013. 3621, 3622, 3628, 3629, 3632, 3633
De Angelis, H. and Skvarca, P.: Glacier surge after ice shelf collapse, Science, 299, 1560–1562, 2003. 3619

TCD
9, 3617–3660, 2015

A new methodology to simulate subglacial deformation

A. Damsgaard et al.

Dewhurst, D. N., Brown, K. M., Clennell, M. B., and Westbrook, G. K.: A comparison of the fabric and permeability anisotropy of consolidated and sheared silty clay, Eng. Geol., 42, 253–267, 1996. 3634

Di Felice, R.: The voidage function for fluid-particle interaction systems, Int. J. Multiphas. Flow, 20, 153–159, 1994. 3626

Dupont, T. K. and Alley, R. B.: Assessment of the importance of ice-shelf buttressing to ice-sheet flow, Geophys. Res. Lett., 32, L04503, doi:10.1029/2004GL022024, 2005. 3619

Engelhardt, H. and Kamb, B.: Basal sliding of ice stream B, West Antarctica, J. Glaciol., 44, 223–230, 1998. 3634, 3635

Ergun, S.: Fluid flow through packed columns, Chem. Eng. Prog., 43, 89–94, 1952. 3626

Feng, Y. Q. and Yu, A. B.: Assessment of model formulations in the discrete particle simulation of gas-solid flow, Ind. Eng. Chem., 43, 8378–8390, 2004. 3620, 3626

Ferziger, J. H. and Perić, M.: Computational Methods for Fluid Dynamics, vol. 3, Springer, Berlin, 2002. 3624

Fischer, U. H. and Clarke, G. K. C.: Review of subglacial hydro-mechanical coupling: Trapridge glacier, Yukon Territory, Canada, Quatern. Int., 86, 29–43, 2001. 3619

Fischer, U. H., Porter, P. R., Schuler, T., Evans, A. J., and Gudmundsson, G. H.: Hydraulic and mechanical properties of glacial sediments beneath Unteraargletscher, Switzerland: implications for glacier basal motion, Hydrol. Process., 15, 3525–3540, 2001. 3620

Fowler, A. C.: An instability mechanism for drumlin formation, Geol. Soc., London, Spec. Pub., 176, 307–319, 2000. 3620

GDR-MiDi: On dense granular flows, Eur. Phys. J. E, 14, 341–365, 2004. 3621, 3629, 3630, 3632

Gerya, T.: Introduction to Numerical Geodynamic Modelling, Cambridge University Press, Cambridge, 2010. 3624

Gidaspow, D.: Multiphase Flow and Fluidization, Academic Press, San Diego, 1994. 3623

Gidaspow, D., Bezburuah, R., and Ding, J.: Hydrodynamics of circulating fluidized beds: kinetic theory approach, Tech. rep., Illinois Inst. of Tech., Dept. of Chemical Engineering, Chicago, IL (United States), 1992. 3620, 3626

Goren, L., Aharonov, E., Sparks, D., and Toussaint, R.: The mechanical coupling of fluid-filled granular material under shear, Pure Appl. Geophys., 168, 2289–2323, 2011. 3621, 3623, 3624, 3633

Gu, Y., Chialvo, S., and Sundaresan, S.: Rheology of cohesive granular materials across multiple dense-flow regimes, Phys. Rev. E, 90, 032206, doi:10.1103/PhysRevE.90.032206, 2014. 3629

Harleman, D. R. F., Mehlhorn, P. F., and Rumer, R. R.: Dispersion-permeability correlation in porous media, J. Hydr. Eng. Div.-ASCE, 89, 67–85, 1963. 3625

Hazen, A.: Discussion of dams on sand formation, T. Am. Soc. Civ. Eng., 73, 199–221, 1911. 3625

Henderson, A., Ahrens, J., and Law, C.: The ParaView Guide, Kitware, Clifton Park, NY, 2007. 3627

Hindmarsh, R. C. A.: The stability of a viscous till sheet coupled with ice flow, considered at wavelengths less than the ice thickness, J. Glaciol., 44, 285–292, 1998. 3620

Hooke, R. L. and Iverson, N. R.: Grain-size distribution in deforming subglacial tills: role of grain fracture, Geology, 23, 57–60, 1995. 3628

Hoomans, B. P. B., Kuipers, J. A. M., Briels, W. J., and Van Swaaij, W. P. M.: Discrete particle simulation of bubble and slug formation in a two-dimensional gas-fluidised bed: a hard-sphere approach, Chem. Eng. Sci., 51, 99–118, 1996. 3620

Hunter, J. D.: Matplotlib: a 2D graphics environment, Comput. Sci. Eng., 9, 90–95, 2007. 3627

Hutter, K., Svendsen, B., and Rickenmann, D.: Debris flow modeling: a review, Continuum Mech. Therm., 8, 1–35, 1994. 3621

Iverson, N. R.: Coupling between a glacier and a soft bed: II. Model results, J. Glaciol., 45, 41–53, 1999. 3620

Iverson, N. R.: Shear resistance and continuity of subglacial till: hydrology rules, J. Glaciol., 56, 1104–1114, 2010. 3620, 3632, 3633, 3635

Iverson, N. R., Jansson, P., and Hooke, R. L.: In-situ measurement of the strength of deforming subglacial till, J. Glaciol., 40, 497–503, 1994. 3620, 3632

Iverson, N. R., Hooyer, T. S., and Hooke, R. L.: A laboratory study of sediment deformation: stress heterogeneity and grain-size evolution, Ann. Glaciol., 22, 167–175, 1996. 3628

Iverson, N. R., Baker, R. W., and Hooyer, T. S.: A ring-shear device for the study of till deformation: tests on tills with contrasting clay contents, Quaternary Sci. Rev., 16, 1057–1066, 1997a. 3628, 3634

Iverson, R. M., Reid, M. E., and LaHusen, R. G.: Debris-flow mobilization from landslides, Ann. Rev. Earth Pl. Sc., 25, 85–138, 1997b. 3632, 3633

Iverson, N. R., Hooyer, T. S., and Baker, R. W.: Ring-shear studies of till deformation: Coulomb-plastic behavior and distributed strain in glacier beds, J. Glaciol., 148, 634–642, 1998. 3619, 3620, 3628, 3632, 3657

Jajcevic, D., Siegmann, E., Radeke, C., and Khinast, J. G.: Large-scale CFD–DEM simulations of fluidized granular systems, Chem. Eng. Sci., 98, 298–310, 2013. 3620

Joughin, I., Fahnestock, M., MacAyeal, D., Bamber, J. L., and Gogineni, P.: Observation and analysis of ice flow in the largest Greenland ice stream, J. Geophys. Res.-Atmos., 106, 34021–34034, 2001. 3635

Kamb, B.: Rheological nonlinearity and flow instability in the deforming bed mechanism of ice stream motion, J. Geophys. Res., 96, 16585–16595, 1991. 3619, 3620

Kavanaugh, J. L. and Clarke, G. K. C.: Discrimination of the flow law for subglacial sediment using in situ measurements and an interpretation model, J. Geophys. Res.-Earth, 111, F01002, doi:10.1029/2005JF000346, 2006. 3619, 3620

Kloss, C., Goniva, C., Hager, A., Amberger, S., and Pirker, S.: Models, algorithms and validation for opensource DEM and CFD-DEM, Prog. Comput. Fluid Dy., 12, 140–152, 2012. 3621, 3623

Kozeny, J.: Ueber kapillare Leitung des Wassers im Boden, Sitzber. Aka. Wiss. Wien, 136, 271–306, 1927. 3625

Krumbein, W. C. and Monk, G. D.: Permeability as a function of the size parameters of unconsolidated sand, T. Am. I. Min. Met. Eng., 151, 153–163, 1943. 3625

Kyrke-Smith, T. M., Katz, R. F., and Fowler, A. C.: Subglacial hydrology and the formation of ice streams, P. R. Soc. A, 470, 20130494, doi:10.1098/rspa.2013.0494, 2014. 3628

Luding, S.: Introduction to discrete element methods: basic of contact force models and how to perform the micro-macro transition to continuum theory, Eur. J. Env. Civ. Eng., 12, 785–826, 2008. 3622

MacAyeal, D. R., Bindschadler, R. A., and Scambos, T. A.: Basal friction of Ice Stream E, West Antarctica, J. Glaciol., 41, 247–262, 1995. 3619

Mair, K. and Hazzard, J. F.: Nature of stress accommodation in sheared granular material: insights from 3D numerical modeling, Earth Planet. Sc. Lett., 259, 469–485, 2007. 3628

Mair, K., Frye, K. M., and Marone, C.: Influence of grain characteristics on the friction of granular shear zones, J. Geophys. Res.-Sol. Ea., 107, ECV-4, doi:10.1029/2001JB000516, 2002. 3628

TCD
9, 3617–3660, 2015

A new methodology to simulate subglacial deformation

A. Damsgaard et al.

Title Page
Abstract Introduction
Conclusions References
Tables Figures
◀◀ ▶▶
◀ ▶
Back Close
Full Screen / Esc
Printer-friendly Version
Interactive Discussion

Mangeney, A., Tsimring, L. S., Volfson, D., Aranson, I. S., and Bouchut, F.: Avalanche mobility induced by the presence of an erodible bed and associated entrainment, Geophys. Res. Lett., 34, L22401, doi:10.1029/2007GL031348, 2007. 3621

McNamara, S., Flekkøy, E. G., and Måløy, K. J.: Grains and gas flow: molecular dynamics with hydrodynamic interactions, Phys. Rev. E, 61, 4054–4059, 2000. 3620, 3623, 3624

Mead, W. J.: The geologic role of dilatancy, J. Geol., 33, 685–698, 1925. 3633

Mitchell, J. K. and Soga, K.: Fundamentals of Soil Behavior, Wiley, New York, 2005. 3628, 3629

Moore, P. L. and Iverson, N. R.: Slow episodic shear of granular materials regulated by dilatant strengthening, Geology, 30, 843–846, 2002. 3633

Morgan, J. K.: Numerical simulations of granular shear zones using the distinct element method 2. Effects of particle size distribution and interparticle friction on mechanical behavior, J. Geophys. Res., 104, 2721–2732, 1999. 3628

Mutabaruka, P., Delenne, J.-Y., Soga, K., and Radjai, F.: Initiation of immersed granular avalanches, Phys. Rev. E, 89, 052203, doi:10.1103/PhysRevE.89.052203, 2014. 3620, 3632

NVIDIA: CUDA C Programming Guide, NVIDIA Corporation, Santa Clara, CA, USA, 5.0 edn., 2013. 3627

Pailha, M., Nicolas, M., and Pouliquen, O.: Initiation of underwater granular avalanches: influence of the initial volume fraction, Phys. Fluids, 20, 111701, doi:10.1063/1.3013896, 2008. 3632

Patankar, S. V.: Numerical Heat Transfer and Fluid Flow, CRC Press, Boca Raton, Florida, USA, 1980. 3624

Piotrowski, J. A.: Genesis of the Woodstock drumlin field, southern Ontario, Canada, Boreas, 16, 249–265, 1987. 3634

Piotrowski, J. A., Larsen, N. K., and Junge, F. W.: Reflections on soft subglacial beds as a mosaic of deforming and stable spots, Quaternary Sci. Rev., 23, 993–1000, 2004. 3634

Press, W. H., Teukolsky, S. A., Vetterling, W. T., and Flannery, B. P.: Numerical Recipes 3rd edition: the Art of Scientific Computing, Cambridge University Press, Cambridge, UK, 2007. 3624

Price, S. F., Bindschadler, C. L., Hulbe, C. L., and Blankenship, D. D.: Force balance along an inland tributary and onset to Ice Stream D, West Antarctica, J. Glaciol., 48, 20–30, 2002. 3619

Radjaï, F., and Dubois, F.: Discrete-Element Modeling of Granular Materials, Wiley-Iste, Hoboken, New Jersey, USA, 2011. 3622, 3628

TCD

9, 3617–3660, 2015

Rathbun, A. P., Marone, C., Alley, R. B., and Anandakrishnan, S.: Laboratory study of the frictional rheology of sheared till, J. Geophys. Res., 113, F02020, doi:10.1029/2007JF000815, 2008. 3620

Reynolds, O.: On the dilatancy of media composed of rigid particles in contact, Philos. Mag., 20, 469–481, 1885. 3633

Rignot, E. and Thomas, R. H.: Mass balance of polar ice sheets, Science, 297, 1502–1506, 2002. 3619

Rignot, E., Casassa, G., Gogineni, P., Krabill, W., Rivera, A., and Thomas, R.: Accelerated ice discharge from the Antarctic Peninsula following the collapse of Larsen B ice shelf, Geophys. Res. Lett., 31, L18401, doi:10.1029/2004GL020697, 2004. 3619

Rondon, L., Pouliquen, O., and Aussillous, P.: Granular collapse in a fluid: role of the initial volume fraction, Phys. Fluids, 23, 073301, doi:10.1063/1.3594200, 2011. 3632

Schellart, W. P.: Shear test results for cohesion and friction coefficients for different granular materials: scaling implications for their usage in analogue modelling, Tectonophysics, 324, 1–16, 2000. 3629

Schofield, A. N. and Wroth, P.: Critical State Soil Mechanics, McGraw-Hill, London, 1968. 3633

Schwartz, F. W. and Zhang, H.: Fundamentals of Ground Water, Wiley, New York, 2003. 3625

Sergienko, O. V. and Hindmarsh, R. C. A.: Regular patterns in frictional resistance of ice-stream beds seen by surface data inversion, Science, 342, 1086–1089, 2013. 3619

Stokes, C. R., Clark, C. D., Lian, O. B., and Tulaczyk, S.: Ice stream sticky spots: a review of their identification and influence beneath contemporary and palaeo-ice streams, Earth-Sci. Rev., 81, 217–249, 2007. 3619

Thomas, R., Rignot, E., Casassa, G., Kanagaratnam, P., Acuña, C., Akins, T., Brecher, H., Frederick, E., Gogineni, P., Krabill, W., Manizade, S., Ramamoorthy, H., Rivera, A., Russell, R., Sonntag, J., Swift, R., Yungel, J., and Zwally, J.: Accelerated sea-level rise from West Antarctica, Science, 306, 255–258, 2004. 3635

Thomason, J. F. and Iverson, N. R.: A laboratory study of particle ploughing and pore-pressure feedback: a velocity-weakening mechanism for soft glacier beds, J. Glaciol., 54, 169–181, 2008. 3620

Topin, V., Dubois, F., Monerie, Y., Perales, F., and Wachs, A.: Micro-rheology of dense particulate flows: application to immersed avalanches, J. Non-Newton. Fluid, 166, 63–72, 2011. 3620

Truffer, M., Harrison, W. D., and Echelmeyer, K. A.: Glacier motion dominated by processes deep in underlying till, J. Glaciol., 46, 213–221, 2000. 3620
Tsuji, T., Kawaguchi, T., and Tanaka, T.: Discrete particle simulation of 2-dimensional fluidized-bed, Powder Technol., 77, 79–87, 1993. 3624
Tsuji, Y., Tanaka, T., and Ishida, T.: Lagrangian numerical simulation of plug flow of cohesionless particles in a horizontal pipe, Powder Technol., 71, 239–250, 1992. 3624
Tulaczyk, S.: Ice sliding over weak, fine-grained tills: dependence of ice-till interactions on till granulometry, Geol. Soc. Am. Mem., 337, 159–177, 1999. 3619
Tulaczyk, S., Kamb, W. B., and Engelhardt, H. F.: Basal mechanics of ice stream B, West Antarctica I. Till mechanics, J. Geophys. Res., 105, 463–481, 2000a. 3619, 3620
Tulaczyk, S., Kamb, W. B., and Engelhardt, H. F.: Basal mechanics of ice stream B, West Antarctica II. Undrained plastic-bed model, J. Geophys. Res., 105, 483–494, 2000b. 3619
Turrin, J. B., Forster, R. R., Sauber, J. M., Hall, D. K., and Bruhn, R. L.: Effects of bedrock lithology and subglacial till on the motion of Ruth Glacier, Alaska, deduced from five pulses from 1973 to 2012, J. Glaciol., 60, 771–781, doi:10.3189/2014JoG13J182, 2014. 3619
Wang, B., Chu, K. W., and Yu, A. B.: Numerical study of particle–fluid flow in a hydrocyclone, Ind. Eng. Chem., 46, 4695–4705, 2007. 3621
Wen, C. and Yu, Y.: Mechanics of fluidization, Chem. Eng. Prog., 62, 100–111, 1966. 3626
Whillans, I. M. and van der Veen, C. J.: The role of lateral drag in the dynamics of Ice Stream B, Antarctica, J. Glaciol., 43, 231–237, 1997. 3619
Winberry, J. P., Anandakrishnan, S., Alley, R. B., Bindschadler, R. A., and King, M. A.: Basal mechanics of ice streams: insights from the stick-slip motion of Whillans Ice Stream, West Antarctica, J. Geophys. Res., 114, F01016, doi:10.1029/2008JF001035, 2009. 3620
Xu, B. H. and Yu, A. B.: Numerical simulation of the gas-solid flow in a fluidized bed by combining discrete particle method with computational fluid dynamics, Chem. Eng. Sci., 52, 2785–2809, 1997. 3620, 3623, 3626
Xu, B. H., Feng, Y. Q., Yu, A. B., Chew, S. J., and Zulli, P.: A numerical and experimental study of the gas-solid flow in a fluid bed reactor, Powder Handling and Processing, 13, 71–76, 2001. 3624
Zhou, Z. Y., Kuang, S. B., Chu, K. W., and Yu, A. B.: Discrete particle simulation of particle–fluid flow: model formulations and their applicability, J. Fluid Mech., 661, 482–510, 2010. 3621, 3623, 3626

Zhu, H. P., Zhou, Z. Y., Yang, R. Y., and Yu, A. B.: Discrete particle simulation of particulate systems: theoretical developments, Chem. Eng. Sci., 62, 3378–3396, 2007. 3623, 3624

TCD
9, 3617–3660, 2015

Table 1. Parameter values used for the shear experiments.

Parameter	Symbol	Value
Particle count	N_p	9600
Particle radius	r	0.01 m
Particle normal stiffness	k_n	1.16×10^9 N m^{-1}
Particle tangential stiffness	k_t	1.16×10^9 N m^{-1}
Particle friction coefficient	μ	0.5
Particle density	ρ	2600 kg m^{-3}
Fluid density	ρ_f	1000 kg m^{-3}
Fluid dynamic viscosity	μ_f	1.797×10^{-8} to 1.797×10^{-6} Pa s
Fluid adiabatic compressibility	β_f	1.426×10^{-8} Pa^{-1}
Hydraulic permeability prefactor	k_c	$[3.5 \times 10^{-15}, 3.5 \times 10^{-13}]$ m^2
Normal stress	σ_0	20 kPa
Top wall mass	m_w	280 kg
Gravitational acceleration	g	9.81 m s^{-2}
Spatial domain dimensions	$\boldsymbol{L}$	[0.52, 0.26, 0.55] m
Fluid grid size	$\boldsymbol{n}_f$	[12, 6, 12]
Shear velocity	$\boldsymbol{v}^x_{\text{p, top}}$	2.32×10^{-2} m s^{-1}
Inertia parameter value	I	1.7×10^{-4}
Time step length	Δt	2.14×10^{-7} s
Simulation length	t_{total}	20 s

TCD
9, 3617–3660, 2015

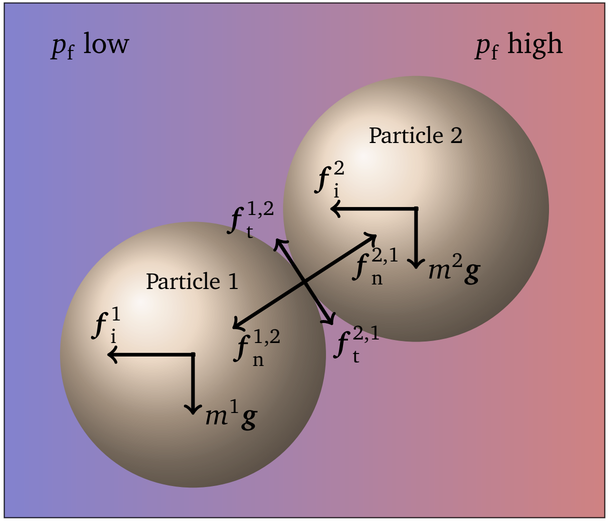

Figure 1. Schematic representation of body and surface forces of two non-rotating and interacting particles submerged in a fluid with a pressure gradient.

TCD
9, 3617–3660, 2015

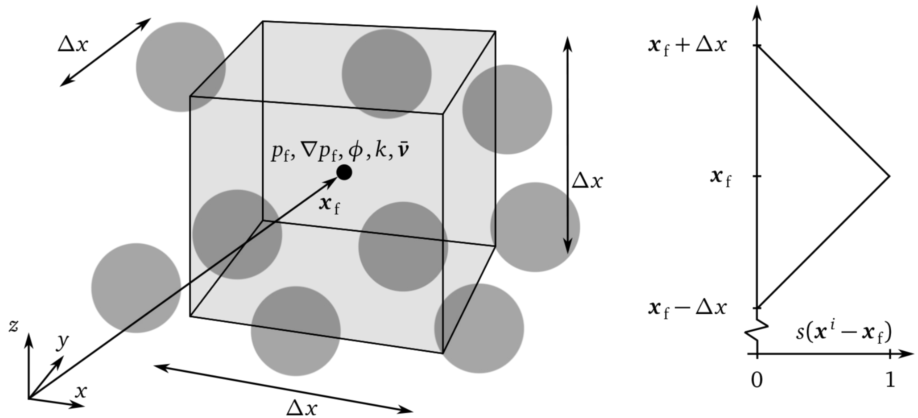

Figure 2. Left: a cell in the fluid grid. The node for pressure (p_f), the gradient of fluid pressure (∇p_f), porosity (ϕ), permeability (k), and average grain velocity ($\overline{v}$) are calculated at the cell center. Right: the weight function (Eq. 7) at various distances.

TCD
9, 3617–3660, 2015

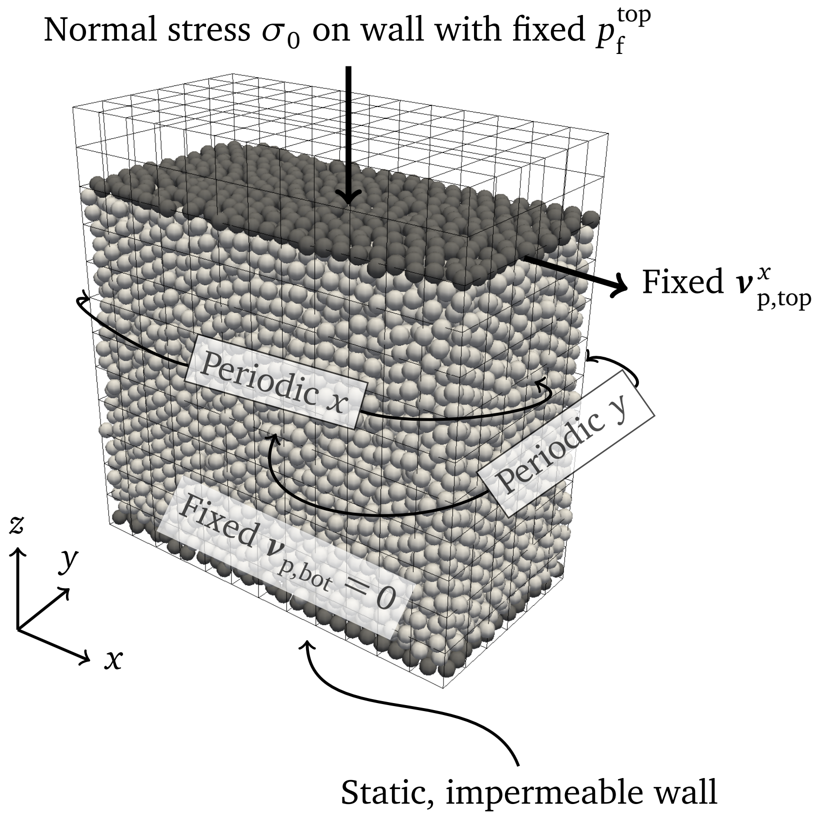

Figure 3. Experimental setup for the shear experiments. The fluid cells containing the mobile top wall are given a prescribed fixed-pressure boundary condition (p_f^{top}, Dirichlet). The bottom boundary is impermeable (no flow, free slip Neumann). The fluid grid is extended upwards to allow for dilation and movement of the upper wall. The granular phase is compressed between a fixed wall at the bottom, and a dynamic top wall, which exerts a normal stress (σ_0) downwards. The material is sheared by moving the topmost particles parallel to the x axis.

TCD
9, 3617–3660, 2015

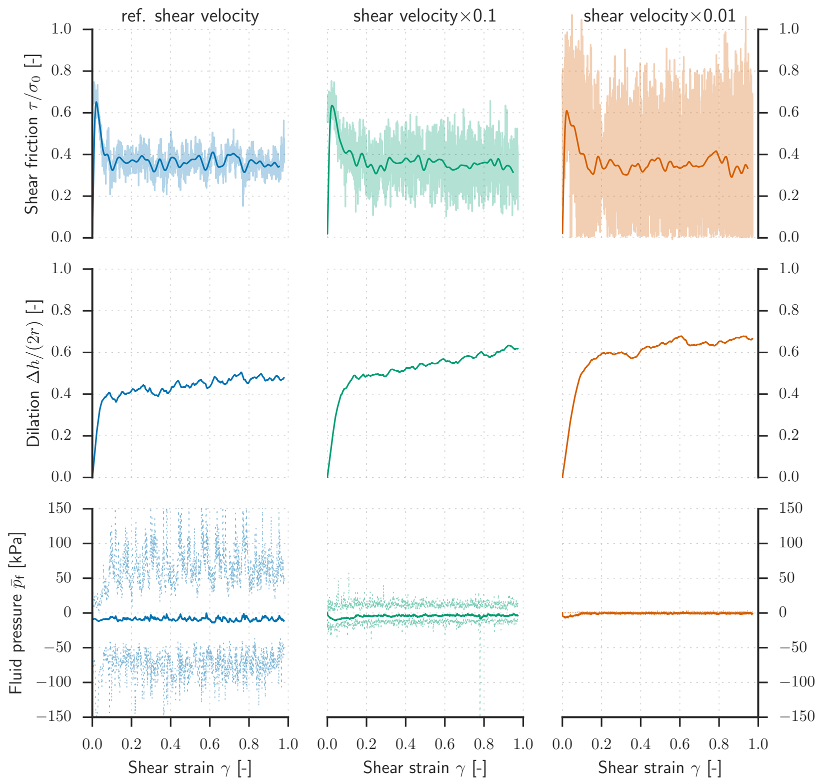

Figure 4. Shear experiments with different shearing rates. (Top) unsmoothed and smoothed shear friction values, (center) dilation in number of grain diameters and (bottom) minimum, mean, and maximum fluid pressures. The permeability prefactor value is $k_c = 3.5 \times 10^{-15}\,\mathrm{m}^2$. The shear friction values (top) are smoothed with a moving Hanning window function to approximate the strength of larger particle assemblages. The material peak strength increases with strain rate due to reductions of internal fluid pressure. This strengthening is taking place when the dilation rate exceeds the dissipation rate of the fluid.

TCD
9, 3617–3660, 2015

A new methodology to simulate subglacial deformation

A. Damsgaard et al.

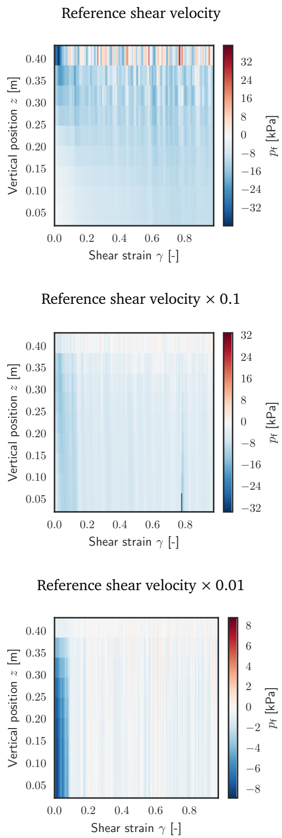

Figure 5. Temporal evolution (x axis) of horizontally averaged fluid pressures (y axis). At fast shear rates (top) there are large internal pressure decreases and slow recovery due to a large dilation rate and an insufficient pressure dissipation. When the shearing velocity is decreased (middle) and (bottom) the dissipation rate becomes increasingly capable of keeping internal pressures close to the hydrostatic pressure (0 kPa).

TCD
9, 3617–3660, 2015

Title Page
Abstract
Introduction
Conclusions
References
Tables
Figures
Back
Close
Full Screen / Esc
Printer-friendly Version
Interactive Discussion

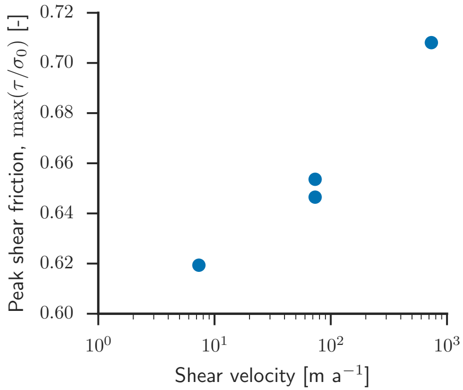

Figure 6. Peak frictional strength before the critical state of the low-permeability granular bed ($k_c = 3.5 \times 10^{-15}\,\mathrm{m}^2$) at different shear velocities. The frictional strength is constant and rate-independent at velocities lower than $10^1\,\mathrm{m\,a}^{-1}$ as pore-pressure diffusion rates far exceed rates in volumetric change.

TCD
9, 3617–3660, 2015

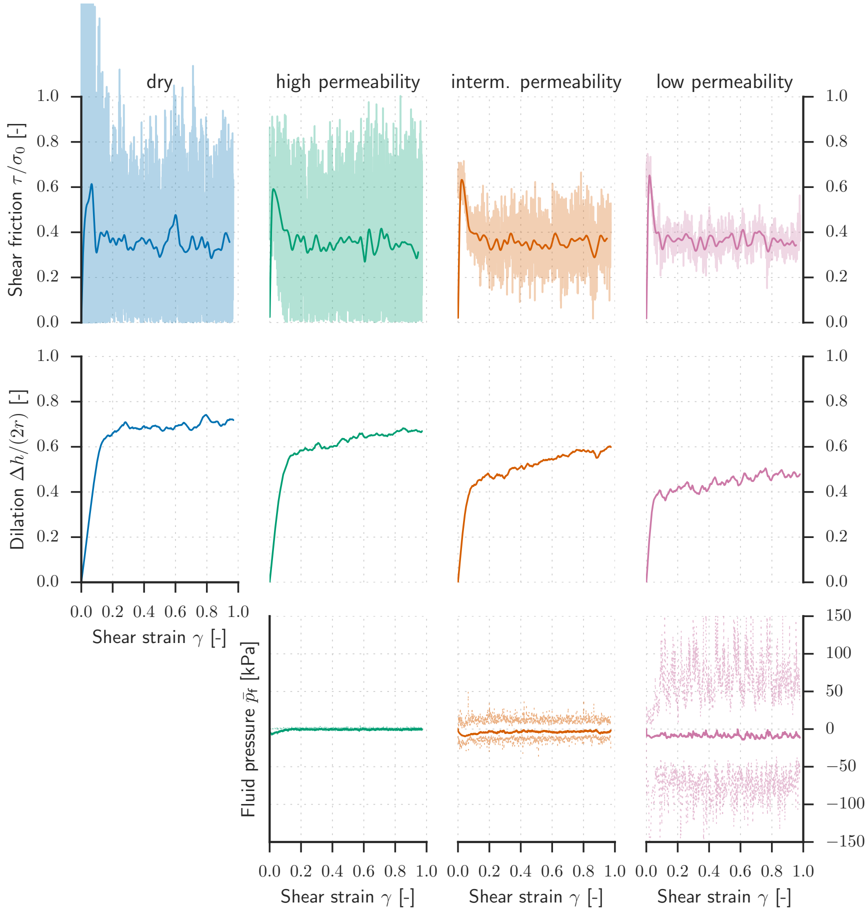

Figure 7. (Top) shear strength, (center) dilation in number of grain diameters and (bottom) minimum, mean and maximum fluid pressures in shear experiments with different permeability properties.

TCD
9, 3617–3660, 2015

A new methodology to simulate subglacial deformation

A. Damsgaard et al.

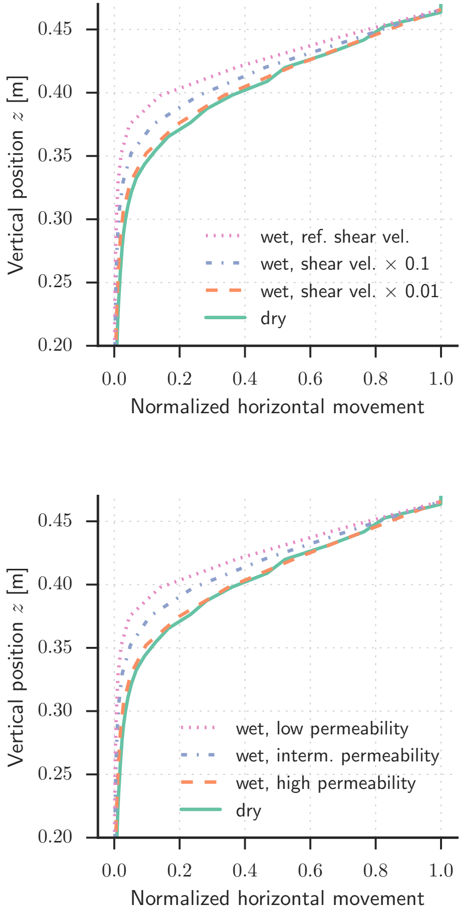

Figure 8. Horizontal particle displacement with depth (shear strain profiles) for the dry and fluid saturated shear experiments. Top: displacement profiles from experiments with different shear velocities. Bottom: displacement profiles from experiments with different permeabilities.

TCD
9, 3617–3660, 2015

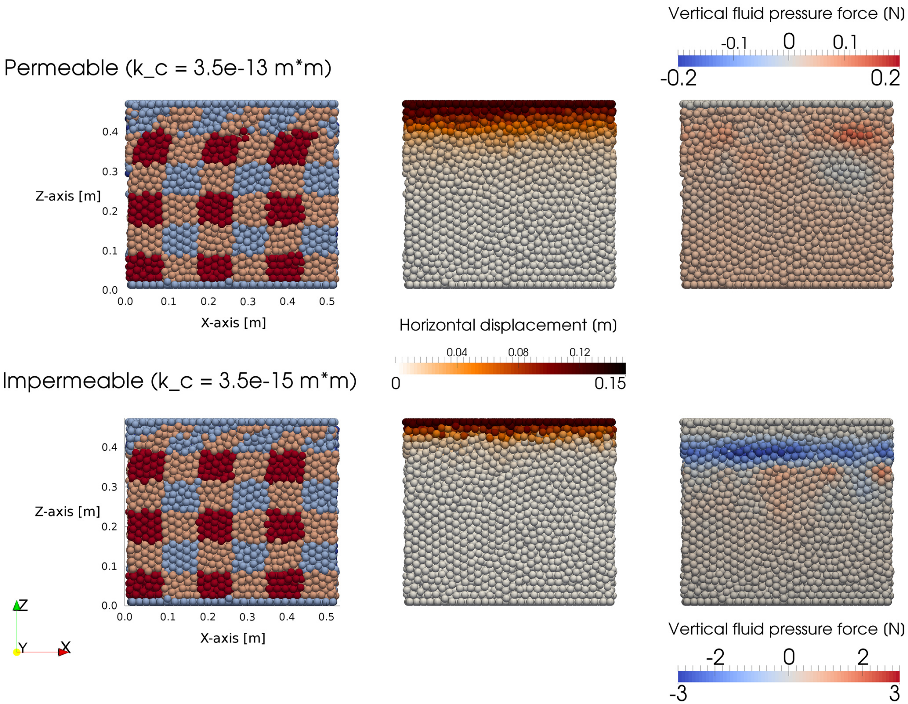

Figure 9. Particle displacement and fluid forces for different permeabilities at a shear strain of 0.25. (Left) particles colored by their original position, (center) particles colored by their displacement along the x axis, (right) vertical (z) forces from the fluid onto the particles. In the permeable material and/or at low shearing velocities (top), the internal volumetric changes are accommodated by porous flow. This keeps the fluid pressures close to hydrostatic values and causes deep deformation (top center). In materials which are impermeable and/or are sheared at fast rates (bottom), the volumetric changes cause drastic pore-pressure reductions, effectively strengthening the material (bottom right) and focusing deformation at the top (bottom left and center).

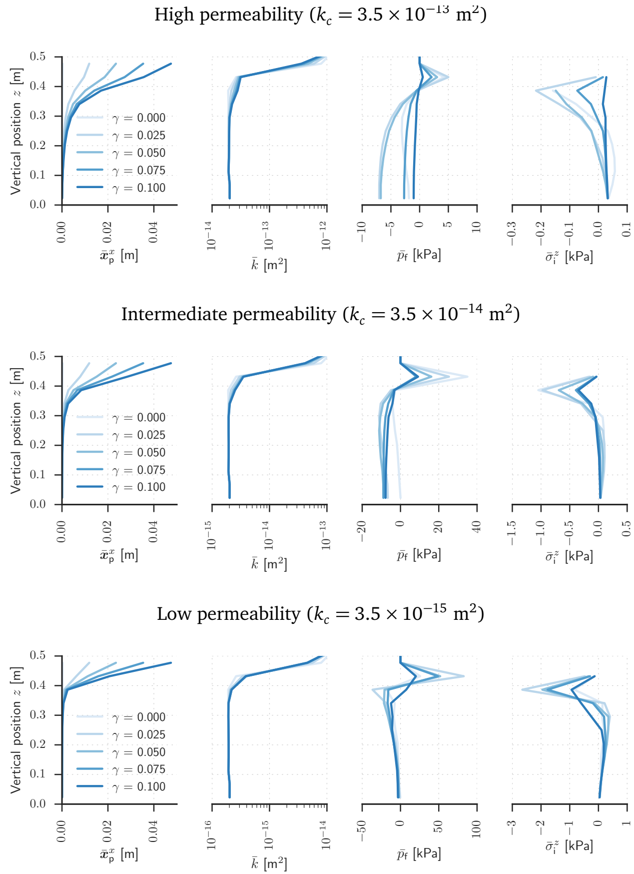

Figure 10. Horizontally averaged fluid and particle behavior with progressive shear strain. (left) Vertical particle displacement, (center left) mean permeability, (center right) mean fluid pressure, and (right) vertical component of the mean fluid stress, calculated as $\boldsymbol{f}_i^i/A^i$, where $\boldsymbol{f}_i^i$ is the fluid pressure force on particle i from Eq. (12) and A^i is its surface area.

TCD
9, 3617–3660, 2015

Title Page
Abstract | Introduction
Conclusions | References
Tables | Figures
◀| |▶
◀ ▶
Back | Close
Full Screen / Esc
Printer-friendly Version
Interactive Discussion

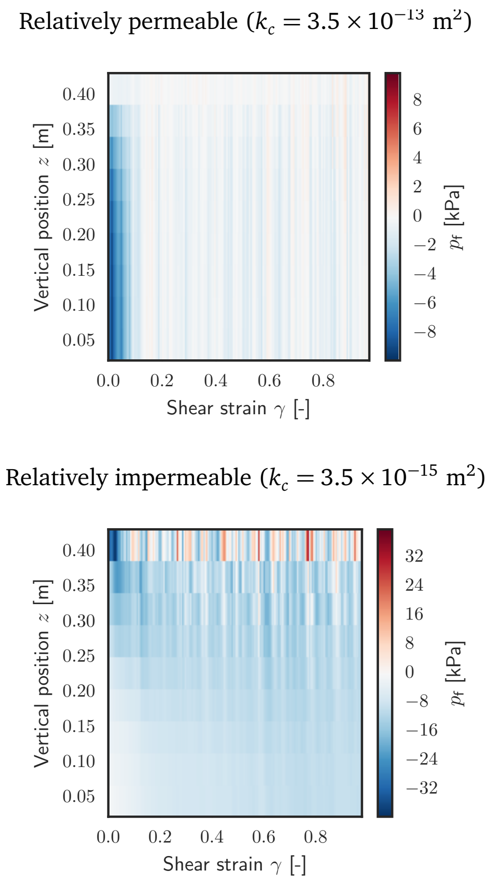

Figure 11. Temporal evolution (x axis) of horizontally averaged fluid pressures (y axis). The permeable material (top) is able to quickly respond to internal volumetric changes, which are short-lived and of small magnitude. The low-permeable material (bottom) is dominated by large pressure reductions and relatively slow relaxation.

TCD
9, 3617–3660, 2015

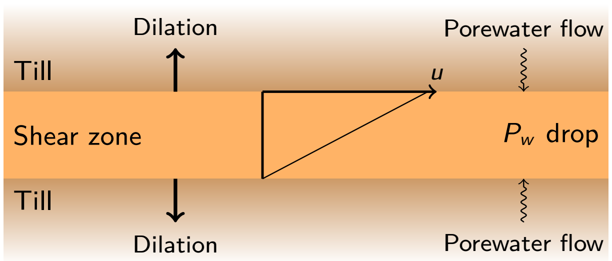

Figure 12. Particle–fluid interaction during deformation of a consolidated sediment. After Iverson et al. (1998).

TCD
9, 3617–3660, 2015

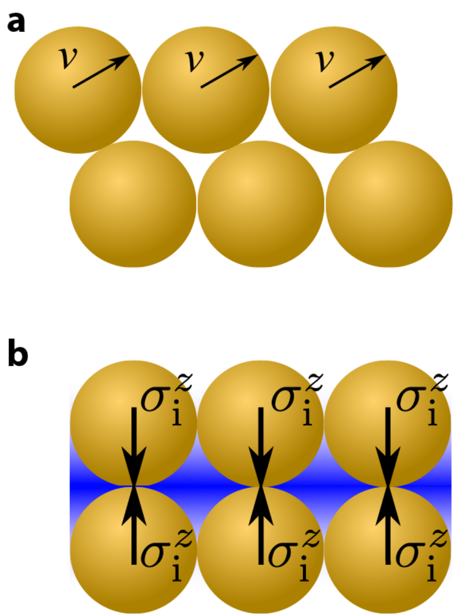

Figure 13. Micro-mechanical cause of dilatant hardening. A consolidated sediment (top) is deformed with a vertical gradient in velocity. The grains are forced past each other in order to accommodate the shear strain. The deformation causes dilation, which increases porosity localy and decreases fluid pressure (bottom). The established gradient in fluid pressure pulls particles together (Eq. 12), which increases the load on inter-particle contacts. The larger inter-particle normal stress increases the shear strength of the contact (Eq. 3) resulting in a stronger sediment.

TCD
9, 3617–3660, 2015

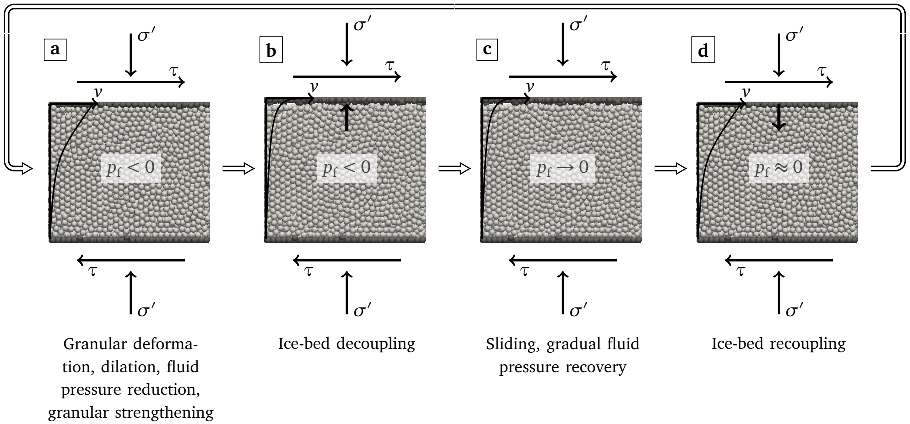

Figure 14. Conceptual model of cyclic strengthening. Feedbacks between sediment and pore-water during shear of a consolidated sediment with low permeability cause strengthening of the sediment during the onset of deformation. The strengthening may cause interfacial decoupling between the glacier and its bed until pore-water pressures in the sediment have recovered. The recoupling causes a new event of deep deformation which yet again causes sediment strengthening.

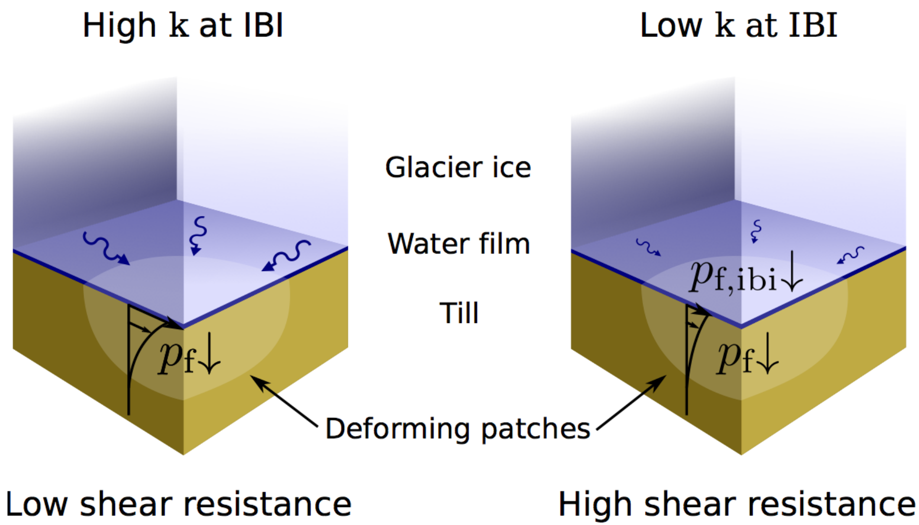

Figure 15. The magnitude of strengthening felt by the glacier due to dilatant hardenining depends on the permeability and water availability at the ice–bed interface (IBI). If the subglacial hydrological system has a high permeability and a thick water film at the IBI (left), the till directly beneath the glacier sole is kept weak because the pore-water pressure is unchanged in the upper-most parts. If the IBI on the other hand has a low permeability and a thin water film (right), the bed strengthens as the volumetric expansion of the till reduces pore-water pressure at all depths.

TCD
9, 3617–3660, 2015